

ARTICLE

OPEN



Morphological and nanomechanical changes in tungsten in high heat flux conditions

Minsuk Seo ¹✉, John R. Echols ² and A. Leigh Winfrey ¹

Morphological and nanomechanical alteration of tungsten in extreme environments, like those in edge localized modes in nuclear fusion environments, up to 46.3 GWm^{-2} heat fluxes were experimentally simulated using electrothermal plasma. Surface and subsurface damage to the tungsten is seen mainly in the form of pore formation, cracks, and resolidified melt instabilities. Micro voids, rosette-type microfeatures, core-shell structure, particle enrichment, and submicron channels all manifest in the damaged subsurface. The formation of voids in the subsurface was determined to originate from the ductile fracture of hot tungsten by plastic flow but not developed to cracking. The voids were preferentially settled in grain boundaries, interfaces. The directionality of elongated voids and grains is biased to the heat flow vector or plasma pathway, which is the likely consequence of the thermally driven grain growth and sliding in the high-temperature conditions. The presence of a border between the transient layer and heat-affected zone is observed and attributed to plasma shock and thermal spallation of fractural tungsten at high temperature. Plasma peening-like hardening effects in tungsten were observed in the range of 22.7 – 46.3 GWm^{-2} but least in the case of the lowest heat flux, 12.5 GWm^{-2} .

npj Materials Degradation (2020)4:30; <https://doi.org/10.1038/s41529-020-00135-4>

INTRODUCTION

Tungsten is a leading material for the divertor of tokamak-style fusion reactors due to its high melting point ($\sim 3422^\circ\text{C}$), good thermal conductivity ($\sim 175 \text{ Wm}^{-1}\text{C}^{-1}$ at room temperature and $\sim 120 \text{ Wm}^{-1}\text{C}^{-1}$ at 800°C), reasonably good mechanical strength ($E_Y \sim 450 \text{ Gpa}$, nanohardness $\sim 8 \text{ GPa}$), high sputtering threshold energy ($E_{th} \sim 200 \text{ eV}$ for deuterium), resistance to hydride formation, and low tritium retention¹. Despite these advantages, there are significant concerns as to the survivability of tungsten in a fusion environment. Damage to tungsten by hydrogen and helium ions, thermal shock from plasma exposure, and high heat effects are all important to understand for predicting the materials performance in nuclear fusion reactor environments^{2–4}.

In particular, an extremely high heat flux environment known as an edge localized mode (ELM)⁵ deliver 1 – 10 GWm^{-2} flux over submillisecond time frames for 10 – 100 sec, and is cause for concern for long term reactor operation. This amount of heat flux is as much as ten million times the intensity of solar radiation ($\sim 1 \text{ kWm}^{-2}$) on the Earth's surface. A laboratory-scale method for physically simulating such high heat flux is by using a capillary discharging device. This device functions through discharging high voltage across a capillary, generates a pulse of electrothermal plasma with density of 10^{23} – 10^{27} m^{-3} , temperature of 1 – 5 eV , particle velocities of $\sim 6 \text{ kms}^{-1}$, pressure of $\sim 300 \text{ MPa}$ ⁶. Previous studies with capillary discharging devices have reached heat flux ranges from 10 to $\sim 140 \text{ GWm}^{-2}$ making them excellent tools for simulating ELM conditions⁷.

Depending upon the heat flux intensity, macroscopic melting can be observed in tungsten plates in fusion reactors⁸. Melting severely damages and loosens the material and can cause tungsten ejection and mass loss from the reactor wall surface^{9,10}. Moreover, resolidified melts deform the plasma contact surface thereby change the operational environment permanently. At the microscopic level, noticeable morphological, phasic, and structural

changes emerge under ELM like conditions^{11–14}. Resolidification of tungsten exposed to ELM condition has been studied¹⁴, but details of morphological changes in surface are still not fully understood. Generally, the resolidification process of plasma exposed molten metals has been widely studied in the field of welding¹⁵. This is the basis for understanding transient melts of tungsten. A high heat flux induced temperature gradient of welded joints is stratified roughly into three zones: the fusion zone, partially melted zone, and heat-affected zone. The fusion zone experiences full melting, whereas the partially melted zone undergoes partial phase change where solid and liquid material coexist briefly. As liquid phase smears into grains, intragranular liquid film separates grains, thereby localizing the tensile stress, which triggers cracking after cooling¹⁶. The heat-affected zone experiences high-temperature conditions but does not undergo melting. Despite the large body of research on welds, the mechanism of phase change related damage in plasma exposed tungsten is not fully understood in the nuclear fusion context.

As fusion energy relies on the deuterium-tritium reaction, which produces helium particles, many studies have been conducted on helium effects in tungsten, particularly the formation of bubbles and nanostructures^{17,18}. Nanostructures form in tungsten where helium energy is higher than 20 eV and temperature are in the 1273 – 2273°C range. Swelling is associated with the coalescence of helium into bubbles, which in turn responsible for embrittlement, and reduction in thermal conductivity. Therefore, mechanical properties such as hardness before and after helium implantation with high radiation damage has been extensively studied by others^{19,20}. In the case of ELM conditions, helium plasma irradiation on tungsten showed that the nanostructures were affected by the high heat load²¹. Collective damage of ELMs and tungsten fuzz effects all lead to erosion²². However, limited numbers of studies have been done on the mechanical properties of tungsten in both high heat flux conditions and with helium

¹Ken and Mary Alice Lindquist Department of Nuclear Engineering, The Pennsylvania State University, University Park, PA 16802, USA. ²Oak Ridge National Laboratory, Oak Ridge, TN 38731, USA. email: mus1507@psu.edu

particle implantation. Also, tungsten behavior in the extreme intensity of high heat fluxes of ELM condition is not well established.

The goal of this study is to understand the damaging mechanisms of material interactions at the tungsten surface in extremely high heat flux, plasma discharge environments, at low contact angle as shown in Fig. 1a. To investigate these mechanisms, morphological changes of the surface and subsurface of samples in Fig. 1b were observed by using focused ion beam (FIB) and scanning electron microscopes (SEM) and behaviors were interpreted based on stopping and range of interaction in matter (SRIM), and nanoindentation measurements.

RESULTS

Morphology

Figure 2 displays morphologies of the surface and subsurface of tungsten as a function of heat fluxes. The observed cracks in

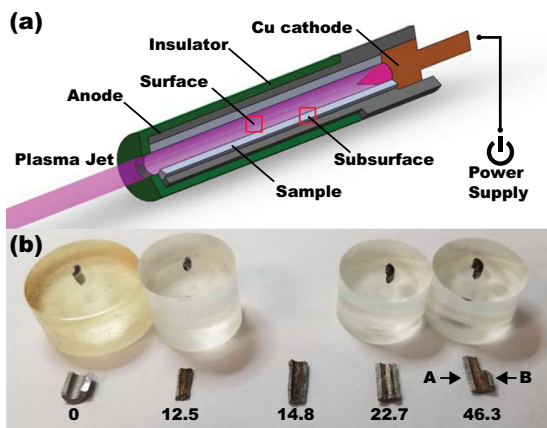


Fig. 1 Image of experimental setups. **a** Simple schematic of a sample loaded HELIOS device. Red boxes indicate the interest regions of measurement. **b** A photograph of undamaged and damaged samples. 46.3 GWm^{-2} observation namely side A and side B. (unit: GWm^{-2}).

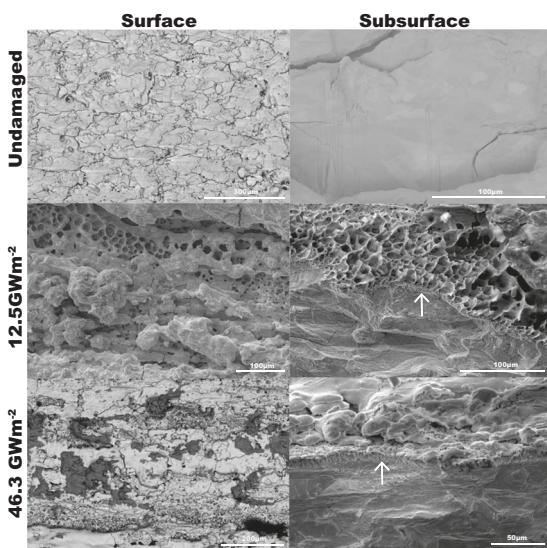


Fig. 2 Surface and subsurface SEM images of undamaged, 12.5 GWm^{-2} damaged, and 46.3 GWm^{-2} damaged samples. Arrows are indicating transient layers.

undamaged surface are likely introduced from the manufacturing process or during mechanical cutting. In the undamaged subsurface, grains of polycrystalline tungsten were revealed by polishing. The 12.5 GWm^{-2} damaged surface has multiple numbers of micron sized pores, located in the resolidified melts. A cross-sectional view of 12.5 GWm^{-2} heat flux exposed sample has cluster of pores with a size of few microns to tens of microns. Some of the resolidified melts were near these pores. There is a recognizable $10\text{-}\mu\text{m}$ thick layer between the porous and the bulk side of the tungsten. Next, a panoramic view of the 46.3 Gm^{-2} damaged surface has tungsten matrix (bright) and copper features (dark) with the size of $50\text{-}100 \mu\text{m}$ implanted from the electrode of HELIOS. Cracks across the surface, micro-size pores, and resolidified melts are irregularly distributed. A cluster of pores on the surface were likely formed by prompt boiling during the moment of plasma interaction. This would imply that temperature was beyond the boiling point of 5930°C and was heterogeneously distributed from the non-uniform nature of the delivered heat flux and/or a fluctuating molten surface. In addition, wrinkles and flow of melts due to the high speed plasma flow can be seen in the resolidified surfaces. These characteristics show a fingerprint for plasma flow direction. This suggests a relatively slow cooling rate, and a viscosity high enough to retain fluidity during cooling.

The cross section of damaged tungsten shows three layers; namely, a resolidified zone, an intermediate layer, and the bulk tungsten. Several tens of μm thick resolidified melts lie on the top of the damaged surface. It is hard to tell the uniformity of thickness due to the fluidic melt behavior. About a $10\text{-}\mu\text{m}$ thick transient layer was observed below the resolidified melts and is uniformly distributed over the subsurface. A cross-sectional view of bulk tungsten implies sporadic macroscopic cracks may be introduced during the plasma exposure or from the manual cutting process. A closer look at this 46.3 GWm^{-2} damaged transient layer on the side labeled "A" in Fig. 1b is displayed in Fig. 3 with EDS results. The analysis revealed fine microfeatures including voids, particulates in the matrix, different shapes and sizes of grains with biased orientations, and a noticeable horizontal border. EDS results of tungsten and copper in the red box of the SEM image show most of the copper atoms were localized about $5 \mu\text{m}$ above the horizontal border of the damaged

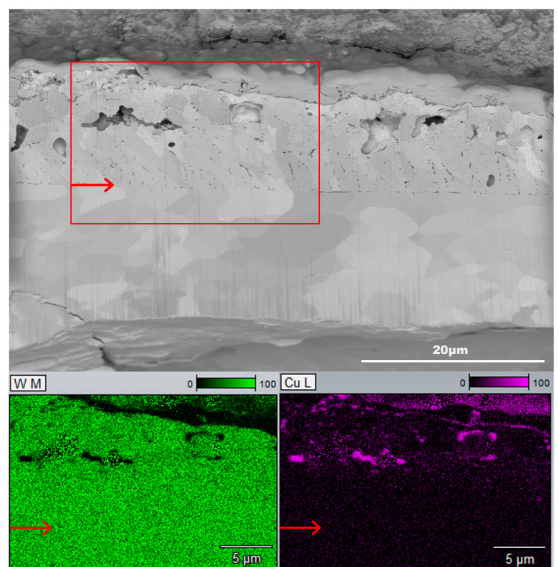


Fig. 3 FIB polished SEM image of side A of 46.3 GWm^{-2} damaged tungsten. EDS maps of tungsten, copper results in a corresponding red box are displayed. Two red arrows indicate the bottom edge border in the SEM image to referring a penetration depth.

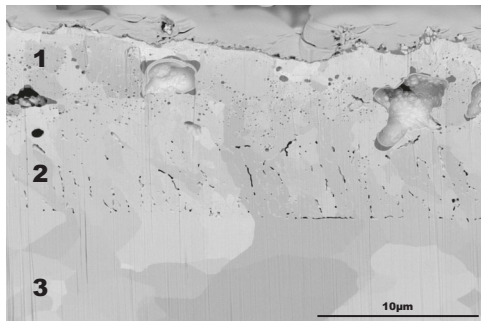


Fig. 4 SEM image of a closer look at of 46.3 GWm^{-2} damaged tungsten in Fig. 5. Layer 1 the fusion zone or resolidified melts, layer 2 the partially melted zone, and layer 3 the heat-affected zone.

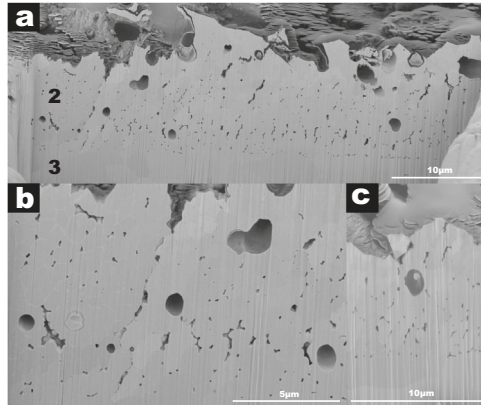


Fig. 5 Cross-sectional SEM images of side B of 46.3 GWm^{-2} damaged tungsten. **a** FIB polished transient layer showing layer 2 and layer 3. **b** Closer look at of the layer showing partially melted zone with grain boundary liquid in the left side face, a thread of sausage-like voids in the middle left, micro-size cavities. **c** An egg-type tungsten core copper shell microparticle.

layer, which is indicated by the red arrow. The portion that was not covered by the tungsten and copper in EDS maps is a carbon layer for FIB treatment. A more detailed SEM image is shown in Fig. 4 to clarify the transient layer of Fig. 3. The transient layer not only appears in Fig. 3 of the 46.3 GWm^{-2} exposure, but also in Fig. 5, meaning that this damage is not region specific. A transient layer is divided into an upper 5 μm or greater thickness region (layer 1), a lower 5–10 μm region (layer 2), and base tungsten (layer 3). Layer 1 contains a couple of μm -size voids, dispersed nano-to-micro-size particulates, irregular patterns of resolidified melts, intergranular nanochannels, and dendrite microfeatures of grains. Scattered nanospheres are copper enrichments according to EDS results. Copper enrichment is mostly located at the interface of two different grains throughout the entire matrix. In line with copper positioning, some of the copper atoms were condensed at the corner of voids. The shape of resolidified melts was like a river delta by making local grains as islands. The feature of these spotted phases is sometimes more like a rosette shape rather than a thinner dendrite. The nanochannels link previously liquified material in the dendrites to the long strand of resolidified melts. It is observable that the copper nanoparticles mostly dwell in that stream of resolidified melts, thus giving an indication for how far and fine melts penetrated in the matrix. Layer 2 is with voids at a triple junction. A vertical strand of sausage-like voids with copper particulates extended across the transient layer alongside the 1–2 μm -sized cavity all describing the bigger size voids was preferred.

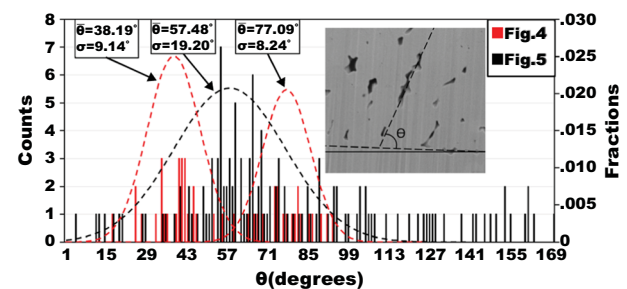


Fig. 6 The angular patterns of voids in Figs. 4 and 5. Inset image shows an example of an estimation of angle θ between the horizontal dashed line (border of layer 2 and layer 3) and void in layer 2. Curves are fitted Gaussian distribution.

Figure 5c shows an egg-shaped tungsten core copper shell microfeature about the size of 2 μm . The border of layer 2 and layer 3 has a bubbly line across the entire sample that clearly divides the transient layer and base tungsten. Layer 3 showed equiaxial grains and no visible voids within. Undamaged tungsten has a grain size of $2.28 \pm 0.43 \mu\text{m}$ while 46.3 GWm^{-2} damaged sample showed $4.37 \pm 0.45 \mu\text{m}$, about a 90% increase in size. The average grain size of the transient layer between layer 1 and layer 2 is $0.85 \pm 0.08 \mu\text{m}$ as can be seen in Fig. 5b. The grain size has decreased by about 67.2, 80.5% compared to layer 3 and undamaged tungsten, respectively.

Void directionality

The angular distribution of voids in layer 2 of Figs. 4 and 5a and presented in Fig. 6. For the voids in Fig. 4, the results are fitted to Gaussian distribution with a broad range from 17° to 93° but with two different peaks. One sits at an average of 38.19° with a standard deviation of 9.14° and the other curve at an average of 77.09° with a standard deviation of 8.24° . A rough cutoff angle between two Gaussian distributions is at 59° , which divides 47 counts into a lower angle group for 27 voids whereas 20 voids grouped in a higher angle. In the case of Fig. 5a, 133 voids out of 220 voids were scattered with orientation from 4° to 169° corresponding 60% chance of having directionality. The Gaussian pattern closely fitted to the angles from 4° to 93° where the average angle is 57.48° with a standard deviation of 19.2° . It is also observable that the multiple voids sitting at higher angles ($>93^\circ$) still counted meaningfully. The average of two curves in Fig. 4 is 54.75° that closely matches with the average angle 57.48° in Fig. 5a.

Nanomechanical properties

Table 1 listed measured nanoindentation and Young's modulus information. Figure 7 shows the decreasing pattern of nanohardness and fluctuating Young's modulus along the distance. Nanohardness decreased 38.8% for the 12.5 GWm^{-2} damaged sample and 24.0% for 46.3 GWm^{-2} damaged one from the transient layer to 1265 μm in depth. Likewise, Young's modulus decreased to 6.8, 3.3% for 12.5 GWm^{-2} , 46.3 GWm^{-2} damaged sample from the transient layer to 1265 μm , respectively. Most of the nanomechanical properties of samples and positions are showing a hardening effect relative to the undamaged sample. However, the 12.5 GWm^{-2} exposure's damaged spot at 1265 μm has nanoindentation 12.3% lower than the value of undamaged sample.

SRIM

Ion distribution of 5 keV helium and copper plasma in molten tungsten with a 1° incident angle is shown in Fig. 8. Figure 8a shows the ion range of helium and its farthest traveled length to

Table 1. Nanomechanical properties of different heat fluxes as a function of depth distance.

Properties	Heat fluxes (GWm^{-2})	Distance (μm)						
		0	25	115	215	415	815	1265
Nanohardness (GPa)	0	10.6 \pm 1.4						
	12.5	15.2 \pm 3.1	11.4 \pm 1.1	12.3 \pm 1.3	11.0 \pm 0.7	11.4 \pm 1.6	11.9 \pm 1.2	9.3 \pm 1.0
	22.7	—	13.0 \pm 1.8	11.5 \pm 1.7	11.6 \pm 0.9	11.5 \pm 1.3	12.2 \pm 1.2	11.4 \pm 1.4
	46.3	15.0 \pm 2.5	12.9 \pm 1.3	12.0 \pm 1.1	12.4 \pm 1.1	12.0 \pm 1.2	11.9 \pm 2.2	11.4 \pm 1.5
Young's Modulus (GPa)	0	342.7 \pm 15.5						
	12.5	359.5 \pm 41.4	360.8 \pm 27.4	384.2 \pm 18.5	343.5 \pm 21.4	359.0 \pm 30.2	373.8 \pm 28.3	334.9 \pm 26.6
	22.7	—	366.6 \pm 35.2	360.5 \pm 30.4	360.2 \pm 26.5	352.8 \pm 30.0	376.1 \pm 29.4	353.7 \pm 29.5
	46.3	363.1 \pm 41.3	370.9 \pm 34.1	354.5 \pm 28.3	360.6 \pm 22.0	358.3 \pm 21.7	358.4 \pm 30.8	351.2 \pm 23.1

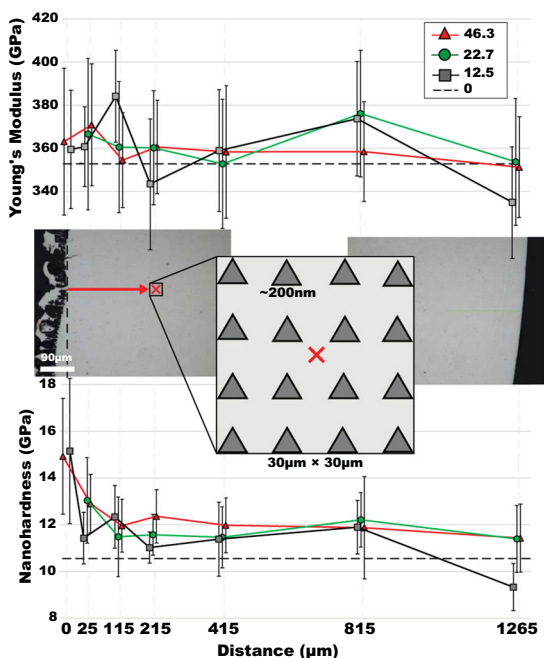


Fig. 7 Patterns of nanoindentation information of undamaged, 12.5, 22.7, and 46.3 (GWm^{-2}) damaged samples as a function of distance. Values in same distance are slightly shifted for clarity. (left) Optical microscope surface images of near edge and (right) far edge are presented alongside the indentation positions. (middle) Cross in a box indicates the location of distance measurement. Dashed lines are the values of the undamaged sample. Error bars represent standard deviation.

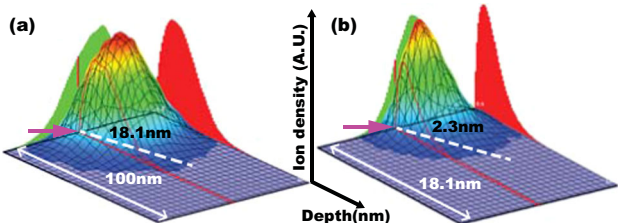


Fig. 8 Ion distribution of 100,000 incidences of 5 keV plasma using SRIM. **a** Helium and **b** copper in liquid tungsten with 1° impact angle. Pink arrows indicate the incoming plasma, black arrows indicate the ion range (peak locations), and dashed lines show skewed pathway. Vertical axis is ion density with arbitrary unit usually ions cm^{-3} .

be 18.1 nm and \sim 50 nm, respectively. Figure 8b shows the ion range of copper and its farthest penetration length to be 2.3 nm, \sim 9 nm, respectively. This indicates that high-Z tungsten would easily hamper the particles. The level of radiation damage from bombarding plasma here would far exceed the melting limit of the lattice. Asymmetry of the ion distribution with respect to the normal vector of surface is due to the low angle bombardment. Since ions travel three order of magnitude less than the thickness of transient layer (\sim 50 μm), initial kinematics cannot allow particles past the 50 μm depth.

DISCUSSION

A descriptive and inclusive damage process of tungsten by plasma and high heat fluxes in extreme ELMs (46.3 GWm^{-2}) is illustrated in Fig. 9. The first interaction of tungsten with plasma is melting. A fluidic behavior of tungsten melts is governed by Raleigh Taylor and Kelvin Helmholtz instabilities such that waves of melts wobble on the viscous surface²³. Raleigh Taylor instability is for normal directional forces acting on the liquid surface while Kelvin Helmholtz instability is for shear caused by high velocity plasma to the surface. These melt instabilities are undesirable in real operation since they alter the surface properties of tungsten significantly unless effectively healed. On top of that, the boiling of tungsten and copper is possible due to the high-temperature condition thus leading to surface instability. The formation of isolated copper regions is due to the immiscibility of copper and tungsten in any temperatures of compositional ranges based on the Cu-W phase diagram. Based on the Hume-Rothery rule, the ionic radius of copper is 1.57 Å while tungsten is 2.07 Å so that 22% of dimensional difference hampers the alloying. Also, the bcc structure of the tungsten and fcc structure of copper are unfavorable to form an intermetallic compound. Furthermore, 36.6 kJmol^{-1} of high positive enthalpy of mixing between tungsten makes insolubility of two metals²⁴. Macroscopic cracking on the surface is due to the rapid solidification of melts as the cooling time is slower than the time of liquid relaxation thus tensile stress remained²⁵. Unrelaxed structures remain and follow Griffith theory-based crack propagation at low temperatures where tungsten is brittle.

The subsurface damage is much more complicated as stratified interactions take place over the depth dimension before and after the damage process. Layer 1 can be considered as similar to the welding fusion zone and the melt pool hence having lowest viscosity compared to other layers during the damage process. As soon as the body cools down, layer 1 experiences accompanying nucleation and growth of new grains governed by shear stress, time during solidification, and cooling rate accounts for the formation of rosette and dendrite microfeatures²⁶. The microstructural evolution at near melting point and quenching was previously investigated by MD simulation²⁷. For example, partial

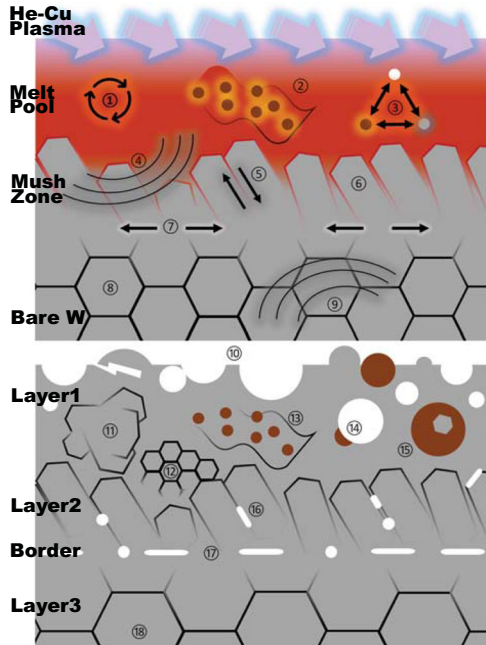


Fig. 9 The mechanisms of morphological changes in melt (top) and resolidified (bottom) tungsten subsurface. (1) melt instability, (2) Cu transport, (3) W(gray)-Cu(brown)-voids(white) interaction, (4) shock wave, (5) grain boundary sliding, (6) grain growth, (7) tensile stress, (8) undamaged grain, (9) compressive stress. (10) pores and cracks, (11) rosette and dendrite microfeatures, (12) refined grains, (13) microchannel, (14) Cu-void, (15) W-Cu core-shell, (16) grain boundary voids, (17) spalled border, and (18) grain growth.

nucleation of a disordered structure coexists with solid state tungsten dependent upon the holding duration at 4273 °C. Quenching triggers either crystallization of melts or amorphization. Remnant microfeatures have remained in transient layers as a snapshot in Figs. 4 and 5. Similar resolidified microfeatures in ELM conditions were evaluated by others¹¹. With the temperature near at melting point and sweeping plasma, the transient layer possibly undergoes ductile fracture by plastic flow. First, voids nucleate at inclusions sites, such as impurities, and interfaces in tungsten, and continue to grow by plasticity. The nucleation of voids at 3073 °C with shear stress obeys a simple relation of gas free void nucleation²⁸:

$$r_c = \frac{2\gamma}{\sigma} \quad (1)$$

where r_c is a critical radius, γ is the surface energy and σ is applied stress. As voids size exceeds than the critical radius, nucleation turns into growth. A continuously applied shear then triggers voids to coarsening and leads to crack formation. However, unlike the surface damage, subsurface does not show any major cracks. Despite the void size seen in the SEM images, the linkages between voids that potentially become a seed for the cracking are yet to be found²⁹. Copper-localized sites can act as void nucleation sites since they provide an interface as shown in Fig. 3. However, the heterogeneous void nucleation and growth were preferable since the temperature of subsurface dropped from the melting points with a relatively long duration that gives a chance for voids to migrate to nucleation sites. Because of the short stopping range of helium and copper in tungsten, their transport should have been assisted by fluidic transportation in nanochannels as copper halted in the middle of the transient layer. This indicates a gradual change of viscosity and permeability along the temperature gradient or depth.

Layer 2 is an intermediate layer with a higher solid fraction in the semi-solid slurry with relatively high viscosity. It is inappropriate to set an exact border between layer 1 and layer 2 because of the vagueness in the boundary. The deformation of dendrite microfeatures readily occurs by showing thixotropic behavior in the mush zone³⁰. A mush zone is a feature found in castings of molten metal characterized by a formation of dendrite network in higher solid fraction at the dendrite coherence point. Figure 5a shows a similar but slightly wider transient layer compared to Fig. 4, which indicates the inequality of plasma damage from region to region. Melts from layer 1 were smeared into preexisting grain boundaries and grain interior¹⁷. Likewise, the columnar grains were preferentially grown to the melted zone in the welded tungsten³¹. Temperature gradient influenced grains in layer 2 were tilted but not layer 1 because of the higher viscosity. For example, the viscosity of tungsten temperature from 3000 °C to the melting point is 10–5 mPas³². Melt instability also easily erases the patterns of directionality information whereas in layer 2 the heat source direction remains, meaning that the directionality of grains in a certain layer may belong to the flexibility or robustness of grains against the external thermal energy. Yet the duration of exposure was not enough to alter the grains to fully align with the heat source direction but the angle of voids sway at 57°. Also, the skewed pathway of plasma in the tungsten body as shown in Fig. 8 is responsible for the heat source direction. The angle varies due to multiple factors such as the variance of plasma intensity, deviation in the duration of interaction, and the morpho-chemical environment. Like layer 1, the origin of micro to submicron size voids in layer 2 is due to the shear and thermal stress-induced void formation but with smaller size, likely because the plasma-induced plastic flow is not as intense as the layer 1. It is unclear if helium was able to travel down to the voids in layer 2 but helium or possibly voids would prefer to settle down the elongated layers and interfaces³³. Grain boundary sliding at an arbitrary boundary can occur due to the local stress concentration in layer 2. The triple junction of the grain boundary is the place where stress builds up by grain boundary sliding induced dislocation emission under high-stress loading³⁴. The grain boundary gets weak as temperature goes up due to easier vacancy migration and a decrease of strength of the material.

Figure 5c shows immiscible copper and tungsten can form an egg-like core-shell microfeatures in the liquid state according to the Marangoni effect³⁵. As the minor liquid phase always forms the core of the egg, the enrichment of copper in a specific region is necessary. The tendency does harmonize with the copper chunk formation in Figs. 2 and 3. The formation of the core-shell structure is based on the surface energy difference between copper and tungsten phases. Yet the boiling temperature of copper (~2562 °C) is lower than the melting point of tungsten, there will be at least 900 °C temperature difference from the outer shell to the inner core. Although the tungsten droplet formation is less desirable than tungsten absorbing into the matrix, the matrix is no more mobile as it cools down to 2562 °C. Inside the shell, the condition for the volumetric growth speed of the core was faster than the resolidification of copper. The Marangoni movement of droplet velocity in steady state is the following:

$$v \approx \frac{-2r}{3(3\mu_W + 2\mu_{Cu})} \cdot \frac{\partial\sigma}{\partial T} \frac{\partial T}{\partial x} \quad (2)$$

where r is the radius of the droplet, μ_W and μ_{Cu} are the viscosities of the tungsten³² and copper shell, respectively. σ is the interfacial energy, and x is the distance. The interfacial energy between two liquid phases must deal with the formation of the core microstructure. The interfacial energy between two liquid phases in the copper and tungsten binary system is simply proportional

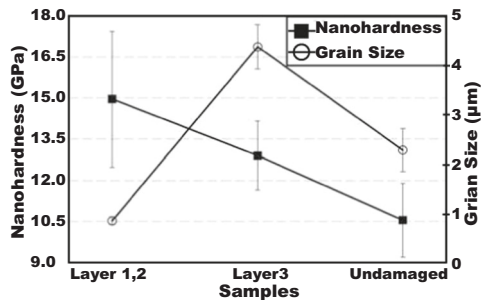


Fig. 10 A comparison of nanohardness and grain size of layer 1 and 2 (transient layer), layer 3, and undamaged samples. Error bars represent standard deviation.

to the square of the concentration difference.

$$\sigma^{L1/L2} \approx \frac{N^* z^*}{N_0 z_0} \cdot L_{CuW} \cdot (C_{Cu}^{L2} - C_{Cu}^{L1})^2 \quad (3)$$

N_0 is Avogadro's number, N^* is the number of front atoms per unit area of the interface, z_0 is the coordination number, z^* is the number of cross bonds per front atom, L_{CuW} is the interaction energy between copper and tungsten, and $(C_{Cu}^{L2} - C_{Cu}^{L1})$ corresponds to the miscibility gap in the liquid phase. The driving force is the interfacial energy between the copper and tungsten liquid phases that is evaluated with the metastable miscibility gap in the copper tungsten binary system. The interfacial energy increases considerably with decreasing temperature because of the large temperature dependence of $(C_{Cu}^{L2} - C_{Cu}^{L1})$. This suggests that if there is a temperature gradient in the droplet, an interfacial tension gradient should also exist. Microchannels are observed in Fig. 4 as a branch of liquid tungsten smeared into subjected grains. Again, copper was transported by the flow of liquid tungsten that is commensurate with particles delivered by microchannel analog to microfluidics of liquid metal³⁶. A combination of tungsten and copper was suggested to use as a thermomechanically improved material. Evidently, nanohardness of tungsten in transient layer is greater than layer 3 and undamaged side as shown in Fig. 10 as hardening effect attributed to accumulation of residual stress, higher void density and clusters of copper nanoparticles.

A border between layer 2 and layer 3 distinguished the transient layer and heat-affected zone. This is shock and thermal induced spallation when laser driven shock wave can introduce a spallation in tungsten³⁷. Shock-induced spallation is possible since HELIOS exerts pressures higher than 100 MPa to the tungsten surface during the plasma exposure. It is also known that yield strength of tungsten weakens at high-temperature ranges and will drop to 100 MPa at near melting point as 2300 °C showed 140 MPa³⁸. Increasing strain and strain rate induces microfractures in tungsten³⁹. Therefore, this border is the place where fractures happen from the exterior tensile stress by a shock wave near melting temperature. That is why SEM images showed a clear distinction between partially melted layer 2 and solid layer 3 in morphology. Thermal spallation might be another reason that gives a border because of the strong temperature and stress gradient along the depth axis⁴⁰. A rapid temperature rises and drop afford to generate thermal stress as different parts of the tungsten expand and shrink. This effect gets severe as the temperature of tungsten drops to ductile to brittle transition temperature acting as like a fragile glass. Fusion relevant transient heat loads on tungsten would lead crack formation by thermal stress⁴¹. The thermal shock brings tensile and compressive stress along the way it propagates then spallation type voids were nucleated and enlarged after the shock.

The heat-affected zone experienced a high temperature but below the melting point. There are no more copper particles that

exist in layer 3, so heat and pressure driven damage is the only factor. The recrystallization temperature of tungsten is around at the range of 1300–1500 °C according to the supplier. Thus, the tungsten grain growth was affordable by comparing the size of the grains in undamaged subsurface of Fig. 2 and 46.3 GWm⁻² damaged subsurface of Fig. 4 possibly accompanying recovery and recrystallization behind. Figure 10 shows a relationship between grain size and nanohardness for each sample but not all samples agree on classical Hall Petch relations:

$$\sigma_Y = \sigma_0 + \frac{k_Y}{\sqrt{D}} \quad (4)$$

where σ_Y is the yield stress, σ_0 is a constant for starting stress causing dislocation movement in tungsten, k_Y is the strengthening coefficient, D is the average grain diameter. Normally yield stress has proportional relations to nanohardness. By comparing layers 1 and 2 to layer 3, nanohardness increased as grain size decreased. However, layer 3 and the heat-affected zone show reverse Hall Petch type relations, which points out that the grain size is not the only factor affecting hardness, rather residual stress such as dislocation density was affected. Although grain size of pristine tungsten is about 100 times larger than the critical grain size (~20 nm) of normally suggested reverse Hall Petch relations in metals³⁴, nanohardness has increased probably because of the accumulated residual stress. As the plasma-induced shock wave propagates to the tungsten sample, residual stress has increased by the formation of dislocations. Simply, the residual stress generation and high-temperature annealing compete together counteractively along the depth dimension. Due to the overwhelming plasma shock-induced hardening over annealing effects, mechanical strength is higher in damaged samples than the undamaged sample. This is similar to the plasma peening process often used to enhance the hardness⁴². Compressive stress and hardening occur as long as the pressure plastically deform the structure⁴³. A higher number of voids in layer 1 and layer 2 impede the propagation of dislocation causing hardening²⁸. The dislocation density in the metal increased by laser shock for the large portion of the body⁴⁴. The intensity of hardness slightly decreases along the distance is due to the heating effects by the shock wave⁴⁵ and diffused over larger volume⁴⁶. The hardening effects turns into softening as high-temperature annealing influenced more than shock peening on 12.5 GWm⁻² damaged sample at 1265 μm meaning that plasma shock decays faster than the mitigation of shock damage along the depth dimension. Higher the heat flux, the more aggressive shock stimulates the more damage.

In conclusion, tungsten was exposed to high heat flux up to 46.3 GWm⁻² in order to investigate ELM-relevant damage in the near surface. The morphological surface damages showed frozen melt instability with high porosity and macro-cracks that originated from the fast-cooled brittle tungsten. Below the surface, resolidified melts (layer 1), partially melted zone (layer 2), and heat-affected zone (layer 3) were found.

- Layer 1 contained rosette-type microfeatures that formed from shear stress, time during solidification, and cooling rate under melt instability. Nanochannels of liquid tungsten transported copper particles of short stopping range to deeper depth. Voids in this layer were formed by plasma and thermal stress assisted nucleation and growth under plasticity but did not evolve to the point of fracture.
- Layer 2 has columnar grains and void directionality aligned to the heat source with an average angle of 57°, determined by the robustness of semi-solid mainly viscosity. Void localization in grain boundaries, stress-induced sliding, and higher mobility by vacancy migration all weaken the material strength in high-temperature conditions. The hardening effect in layer 1 and layer 2 is from to small grain size, copper enrichment, higher void numbers, and residual stress.

- The sharp border between layer 2 and layer 3 showed shock and thermal spallation took place on the fractured tungsten during the damage process.
- In layer 3, grain size has increased compared to the undamaged material through by high-temperature grain growth. Plasma peening-like hardening overwhelmed thermal annealing for all depth dimensions except for the 12.5 GWm^{-2} damaged tungsten at the far edge region.

METHODS

Sample preparations and plasma exposure experiments

The tungsten used in this work were supplied by Midwest Tungsten Service Inc. and machined by the supplier into hollow cylinders, or sleeves, with a 4 mm inner diameter, 6.9 mm outer diameter, and 110 mm in length. The products were manufactured by powder sintering under high temperature and pressure. The sample density is 99.6% theoretical density and compositional purity is 99.95% as shown in Table 2. The sleeve geometry is a requirement for samples installed in the electrothermal plasma generator used for this work, the heat exposure limit, ion outflow system (HELIOS). A schematic of this device is shown in Fig. 1a. Prior to discharge, a capacitor bank is charged to high energy. When discharged, high voltage jumps from the device cathode to anode and this current arc delivers energy to the walls and generates a plume of plasma from the dissociated wall materials. During the plasma exposure experiments, a copper electrode was used and discharges were initiated at room temperature. The device was evacuated and backfilled with helium gas to generate high energy helium. To achieve ELM like conditions, a single 1–2 μs pulse with peak voltages up to 5 kV and maximum currents of 30 kA were applied. Because the exposed surface area is small, high heat loads can be easily achieved. Four separate heat fluxes were investigated: 12.5 GWm^{-2} , 14.8 GWm^{-2} , 22.7 GWm^{-2} , and 46.3 GWm^{-2} . The plasma profiles as a function of time were calculated based on the electrothermal conditions in the previous study⁷. The samples were carefully unloaded after cooling at room temperature and sectioned into smaller pieces for analysis as shown in Fig. 1b. FIB techniques were employed for undamaged and 46.3 GWm^{-2} damaged samples in order to excavate the cross-sectional surface. The grains of undamaged tungsten in Fig. 2 and 46.3 GWm^{-2} damaged tungsten in Figs. 3 and 5 were selected and averaged by using the standard line interpret method to get a representative size. The SEM images were captured using the backscatter detector of a FEI Quanta 200 ESEM and FESEM at 5 keV.

Void directionality

Forty-seven voids in Fig. 4 and 220 voids in Fig. 5a were manually identified and their angles respect to the bottom bubbly border were analyzed, see inset image of Fig. 6. The aspect ratio of voids needed to be at least higher than 2 so that the directionality is recognizable. Tolerance of measurement was 1–2° the slight tilt of the SEM images was accounted for, Figs. 4 and 5a.

Nanoindentation

Nanoindentation was performed on the polished surface in order to quantify the nanomechanical properties by using a Hysitron TI-900 Tribolindenter. The tip is a Berkovich-type indenter with a size of 200 nm. The samples were prepared in solid epoxy resin as shown in Fig. 1b so that the subjected surface is mechanically stable during the indentation. For the undamaged samples, 16 measurements were taken from a wide sampling area to get an average nanomechanical value. For 12.5, 22.7 and 46.3 GWm^{-2} damaged samples, indentations were conducted linearly from 0, 25, 115, 215, 815, and 1265 μm along the depth direction as shown in Fig. 7. The 0 μm site is simply a transient layer. These positions were verified by an optical microscope. For the 0 μm region, indentation was conducted four times to get 16 indentations with 10 μm spacing. For other

M. Seo et al.

bulk side positions, 16 indentations with 10 μm spacing were conducted, and obtained values were averaged. Reduced Young's modulus was calculated:

$$\frac{1}{E^*} = \frac{1 - v^2}{E} + \frac{1 - v^2}{E'} \quad (5)$$

where E^* is reduced Young's modulus, E is the modulus of a specimen, E' is the modulus of the indenter, and v is Poisson's ratio of tungsten 0.28.

SRIM

Stopping and range of interaction in matter (SRIM) was used to understand copper and helium particle collisions with the tungsten matrix, 1×10^5 50 keV copper and helium ions were bombarded on the tungsten sample with low impact angle, 1°, relative to the impact surface. Displacement energy of tungsten was 68 eV and the collision mechanism follows the Kinchin–Pease model. The phase of tungsten would not matter for the simulation nonetheless the density of liquid tungsten is 17.6 gcm^{-3} .

DATA AVAILABILITY

The data that support the findings of this study are available from the corresponding author upon reasonable request.

Received: 26 May 2020; Accepted: 2 September 2020;

Published online: 02 October 2020

REFERENCES

1. Davis, J. W. et al. Assessment of tungsten for use in the ITER plasma facing components. *J. Nucl. Mater.* **258**, 308–312 (1998).
2. Tamura, S. et al. Damage process of high purity tungsten coatings by hydrogen beam heat loads. *J. Nucl. Mater.* **337**, 1043–1047 (2005).
3. Wirtz, M. et al. Thermal shock behaviour of tungsten after high flux H-plasma loading. *J. Nucl. Mater.* **443**, 497–501 (2013).
4. Tokunaga, K. et al. Synergistic effects of high heat loading and helium irradiation of tungsten. *J. Nucl. Mater.* **329–333**, 757–760 (2004).
5. Zohm, H. Edge localized modes (ELMs). *Plasma Phys. Control. Fusion* **38**, 105–128 (1996).
6. Powell, J. D. & Zielinski, A. E. Capillary discharge in the electrothermal gun. *IEEE Trans. Magn.* **29**, 591–596 (1993).
7. Echols, J. R. & Winfrey, A. L. Ablation of fusion materials exposed to high heat flux in an electrothermal plasma discharge as a simulation for hard disruption. *J. Fusion Energy* **33**, 60–67 (2014).
8. Budaev, V. P. et al. Tungsten melting and erosion under plasma heat load in tokamak discharges with disruptions. *Nucl. Mater. Energy* **12**, 418–422 (2017).
9. Federici, G. et al. Effects of ELMs and disruptions on ITER divertor armour materials. *J. Nucl. Mater.* **337–339**, 684–690 (2005).
10. Garkusha, I. E. et al. The latest results from ELM-simulation experiments in plasma accelerators. *Phys. Scr.* **T138**, 014054 (2009).
11. Vilémová, M. et al. Evaluation of surface, microstructure and phase modifications on various tungsten grades induced by pulsed plasma loading. *Phys. Scr.* **91**, 034003 (2016).
12. Bardin, S. et al. Evolution of transiently melt damaged tungsten under ITER-relevant divertor plasma heat loading. *J. Nucl. Mater.* **463**, 193–197 (2015).
13. Wirtz, M. et al. Influence of helium induced nanostructures on the thermal shock performance of tungsten. *Nucl. Mater. Energy* **9**, 177–180 (2016).
14. Hoashi, E. et al. Study on melting and solidification behaviors of tungsten loaded by high heat flux for divertor in tokamak fusion reactor. *Fusion Eng. Des.* **136**, 350–356 (2018).
15. Zhu, T., Chen, Z. W. & Gao, W. Microstructure formation in partially melted zone during gas tungsten arc welding of AZ91 Mg cast alloy. *Mater. Charact.* **59**, 1550–1558 (2008).
16. Kou, S. Solidification and liquation cracking issues in welding. *JOM* **55**, 37–42 (2003).
17. Kajita, S. et al. Formation process of tungsten nanostructure by the exposure to helium plasma under fusion relevant plasma conditions. *Nucl. Fusion* **49**, 095005 (2009).
18. Baldwin, M. J. & Doerner, R. P. Helium induced nanoscopic morphology on tungsten under fusion relevant plasma conditions. *Nucl. Fusion* **48**, 035001 (2008).
19. Armstrong, D. E. J., Edmondson, P. D. & Roberts, S. G. Effects of sequential tungsten and helium ion implantation on nano-indentation hardness of tungsten. *Appl. Phys. Lett.* **102**, 251901 (2013).

Table 2. Chemical impurities in sample according to supplier.

Impurity	O	Ni	N	Fe	P	Si	Ca	Mg	S	Al
Atomic (ppm)	≤ 30	≤ 20	≤ 18	≤ 15	≤ 12	≤ 10	≤ 10	≤ 10	≤ 9	≤ 9

20. Cui, M. et al. He ion implantation induced He bubbles and hardness in tungsten. *Nucl. Mater. Energy* **15**, 232–236 (2018).
21. De Temmerman, G. et al. Helium effects on tungsten under fusion-relevant plasma loading conditions. *J. Nucl. Mater.* **438**, S78–S83 (2013).
22. Sinclair, G., Tripathi, J. K. & Hassanein, A. Erosion dynamics of tungsten fuzz during ELM-like heat loading. *J. Appl. Phys.* **123**, 133302 (2018).
23. Miloshevsky, G. & Hassanein, A. Modeling of macroscopic melt layer splashing during plasma instabilities. *J. Nucl. Mater.* **415**, S74–S77 (2011).
24. Hou, C. et al. W-Cu composites with submicron-and nanostructures: progress and challenges. *NPG Asia Mater.* **11**, 1–20 (2019).
25. Budaev, V. P. et al. Tungsten recrystallization and cracking under ITER-relevant heat loads. *J. Nucl. Mater.* **463**, 237–240 (2015).
26. Flemings, M. C. Solidification processing. *Metall. Trans.* **5**, 2121–2134 (1974).
27. Li, S. et al. Effect of cooling rates on solidification, microstructure and mechanical properties in tungsten. *CrystEngComm* **21**, 3930–3938 (2019).
28. Horacek, O., Toth, C. L. & Horacek, K. Void growth mechanism in bubble strengthened tungsten. *High. Temp. Mater. Process* **13**, 49–60 (1994).
29. Pineau, A., Benzerga, A. A. & Pardoen, T. Failure of metals I: brittle and ductile fracture. *Acta Mater.* **107**, 424–483 (2016).
30. Dahle, A. K. & StJohn, D. H. Rheological behavior of the mushy zone and its effect on the formation of casting defects during solidification. *Acta Mater.* **47**, 31–41 (1998).
31. Cole, N. C., Gilliland, R. G. & Slaughter, G. M. Weldability of tungsten and its alloys. *Weld. J.* **50**, 419-s (1971).
32. Paradis, P. F., Ishikawa, T. & Yoda, S. Viscosity of liquid undercooled tungsten. *J. Appl. Phys.* **97**, 106101 (2005).
33. Chen, D. et al. Self organization of helium precipitates into elongated channels within metal nanolayers. *Sci. Adv.* **3**, eaao2710 (2017).
34. Quek, S. S. et al. The inverse hall-petch relation in nanocrystalline metals: a discrete dislocation dynamics analysis. *J. Mech. Phys. Solids* **88**, 252–266 (2016).
35. Wang, C. P. et al. Formation of immiscible alloy powders with egg-type microstructure. *Science* **297**, 990–993 (2002).
36. Hutter, T. et al. Formation of spherical and non-spherical eutectic gallium-indium liquid-metal microdroplets in microfluidic channels at room temperature. *Adv. Funct. Mater.* **22**, 2624–2631 (2012).
37. Hu, L., Miller, P. & Wang, J. High strain-rate spallation and fracture of tungsten by laser-induced stress waves. *Mater. Sci. Eng. A* **504**, 73–80 (2009).
38. Škoro, G. P. et al. Yield strength of molybdenum, tantalum and tungsten at high rates and very high temperatures. *J. Nucl. Mater.* **425**, 45–51 (2012).
39. Dümmer, T. et al. Effect of strain rate on plastic flow and failure in polycrystalline tungsten. *Acta Mater.* **46**, 6267–6290 (1998).
40. Li, C. et al. Thermal-stress analysis on the crack formation of tungsten during fusion relevant transient heat loads. *Nucl. Mater. Energy* **13**, 68–73 (2017).
41. Li, M., Werner, E. & You, J. H. Influence of heat flux loading patterns on the surface cracking features of tungsten armor under ELM-like thermal shocks. *J. Nucl. Mater.* **457**, 256–265 (2015).
42. Unal, O., Maleki, E. & Varol, R. Effect of sever shot peening and ultra-low temperature plasma nitriding on Ti-6Al-4V alloy. *Vacuum* **150**, 69–78 (2018).
43. Mostafa, A. M., Hameed, M. F. & Obayya, S. S. Effect of laser shock peening on the hardness of AL-7075 alloy. *J. King Saud. Univ. Sci.* **31**, 472–478 (2019).
44. Wang, C. et al. Dislocation density-based study of grain refinement induced by laser shock peening. *Opt. Laser Technol.* **121**, 105827 (2020).
45. Rutkevich, I., Zaretsky, E. & Mond, M. Thermodynamic properties and stability of shock waves in metals. *J. Appl. Phys.* **81**, 7228–7241 (1997).
46. Lake, H. R. *Digital Computer Solution for Propagation of A Spherical Shock Wave in Aluminum* (Oklahoma State University, 1962).

ACKNOWLEDGEMENTS

This manuscript has been authored in part by UT-Battelle, LLC, under Contract No. DE-AC05-00OR22725 with the U.S. DOE. This work was supported by Nuclear Engineering Program at University of Florida, the Kenn and Mary Alice Lindquist Department of Nuclear Engineering at Pennsylvania State University. We are grateful for the professionals in the Materials Research Institute (MRI) at Pennsylvania State University. We are grateful to Dr. Yutai Katoh, Dr. Daniel Morrall in Oak Ridge National Laboratory, and Nathan Reid in University of Illinois at Urbana-Champaign for their helpful comment reviews. This manuscript has been authored in part by UT-Battelle, LLC, under contract DE-AC05-00OR22725 with the US Department of Energy (DOE). The US government retains and the publisher, by accepting the article for publication, acknowledges that the US government retains a nonexclusive, paid-up, irrevocable, worldwide license to publish or reproduce the published form of this manuscript, or allow others to do so, for US government purposes. DOE will provide public access to these results of federally sponsored research in accordance with the DOE Public Access Plan (<http://energy.gov/downloads/doe-public-access-plan>).

AUTHOR CONTRIBUTIONS

M.S. wrote the manuscript and performed the SEM, nanoindentation, characterization, and SRIM work. J.R.E. and A.L.W. performed HELIOS experiments and sample preparation. All the authors contributed in writing and proofreading of the final paper.

COMPETING INTERESTS

The authors declare no competing interests.

ADDITIONAL INFORMATION

Correspondence and requests for materials should be addressed to M.S.

Reprints and permission information is available at <http://www.nature.com/reprints>

Publisher's note Springer Nature remains neutral with regard to jurisdictional claims in published maps and institutional affiliations.



Open Access This article is licensed under a Creative Commons Attribution 4.0 International License, which permits use, sharing, adaptation, distribution and reproduction in any medium or format, as long as you give appropriate credit to the original author(s) and the source, provide a link to the Creative Commons license, and indicate if changes were made. The images or other third party material in this article are included in the article's Creative Commons license, unless indicated otherwise in a credit line to the material. If material is not included in the article's Creative Commons license and your intended use is not permitted by statutory regulation or exceeds the permitted use, you will need to obtain permission directly from the copyright holder. To view a copy of this license, visit <http://creativecommons.org/licenses/by/4.0/>.

© The Author(s) 2020